The Company of
Biologists

RESEARCH ARTICLE

Low kindlin-3 levels in osteoclasts of kindlin-3 hypomorphic mice result in osteopetrosis due to leaky sealing zones

Sarah Klapproth[1], Karsten Richter[2], Clara Türk[3], Theresa Bock[3], Thomas Bromberger[1], Julian Dominik[4,5], Kathrin Huck[6], Kristian Pfaller[7], Michael W. Hess[7], Christoph A. Reichel[4,5], Marcus Krüger[3,8], Inaam A. Nakchbandi[6,9] and Markus Moser[1,9,*]

ABSTRACT

Osteoclasts form special integrin-mediated adhesion structures called sealing zones that enable them to adhere to and resorb bone. Sealing zones consist of densely packed podosomes tightly interconnected by actin fibers. Their formation requires the presence of the hematopoietic integrin regulator kindlin-3 (also known as Fermt3). In this study, we investigated osteoclasts and their adhesion structures in kindlin-3 hypomorphic mice expressing only 5–10% of the kindlin-3 level of wild-type mice. Low kindlin-3 expression reduces integrin activity, results in impaired osteoclast adhesion and signaling, and delays cell spreading. Despite these defects, *in vitro*-generated kindlin-3-hypomorphic osteoclast-like cells arrange their podosomes into adhesion patches and belts, but their podosome and actin organization is abnormal. Remarkably, kindlin-3-hypomorphic osteoclasts form sealing zones when cultured on calcified matrix *in vitro* and on bone surface *in vivo*. However, functional assays, immunohistochemical staining and electron micrographs of bone sections showed that they fail to seal the resorption lacunae properly, which is required for secreted proteinases to digest bone matrix. This results in mild osteopetrosis. Our study reveals a new, hitherto understudied function of kindlin-3 as an essential organizer of integrin-mediated adhesion structures, such as sealing zones.

KEY WORDS: Kindlin-3, Osteoclast, Integrin, Podosome, Sealing zone, Bone resorption

INTRODUCTION

Integrins are a family of ubiquitously expressed adhesion receptors that anchor cells within their ambient extracellular matrix. This task requires the binding of talin and kindlin proteins to the integrin cytoplasmic domain, which then triggers the formation of an active integrin conformation capable of stably binding to the extracellular ligand. In addition, both the talin and kindlin protein families initiate the formation of adhesion complexes that are strongly connected with the actin cytoskeleton and serve as signaling centers of the cell (Calderwood et al., 2013; Moser et al., 2009b).

Integrins are also key adhesion receptors for hematopoietic cells. Many of these cells owe their characteristic properties to the rapid activation of their integrins. For instance, platelets and neutrophils circulate in the blood system in a non-adhesive state but swiftly shift their integrins towards an active state to form platelet aggregates during hemostasis or to enable leukocyte adhesion and extravasation to combat infection. We have previously shown that these processes are very sensitive to a genetic reduction in kindlin-3 (also known as Fermt3) expression (Klapproth et al., 2015). While platelets and neutrophils rely on fast integrin activation, which is also achieved by stoichiometric levels of talin-1 and kindlin-3, other hematopoietic cells, such as macrophages and osteoclasts, remain in tissues for long periods and consequently might be less dependent on rapid integrin activation.

In this study, we therefore focused on how a strong reduction of kindlin-3 expression impacts osteoclast function. Osteoclasts are large multinucleated cells that form by fusion of mononucleated hematopoietic precursors of the myeloid lineage. Their main task is to degrade bone matrix. Therefore, osteoclasts polarize and form large circular adhesion structures, so called sealing zones (Takito et al., 2018). These integrin-mediated adhesion structures form tight contacts with the bone surface and encase the ruffled border, a specialized membrane compartment, which secretes protons and proteinases into the subjacent resorption lacunae to degrade both the mineral and organic bone components. Sealing zones consist of strongly interconnected punctate-like adhesion structures, also known as podosomes. Each podosome comprises a dense actin core surrounded by a ring of integrins and integrin-associated adaptor proteins that connect the adhesion complex with the actin cytoskeleton and thereby provide strong matrix adhesion (Collin et al., 2006; Linder and Aepfelbacher, 2003; Pfaff and Jurdic, 2001; van den Dries et al., 2019).

We have previously shown that, in the absence of kindlin-3, macrophages and osteoclasts can only form immature podosomes consisting of a smaller actin core than normal podosomes and lacking a discrete ring of integrins. The absence of integrin-mediated signaling leads to defects in cytoskeletal organization and cell spreading. Consequently, osteoclasts from kindlin-3-null mice fail to form sealing zones and exhibit strongly reduced bone resorption, which results in a severe osteopetrosis (Schmidt et al., 2011). Osteoblasts do not contribute to the increased bone mass of kindlin-3-knockout mice (Schmidt et al., 2011), because, like osteocytes and chondrocytes, they differentiate from mesenchymal progenitors that only express kindlin-2 (also known as Fermt2) and not kindlin-3. Consistent with this, recent studies in kindlin-2 mutant mice have reported defects in skeletal development, bone

[1]Institute of Experimental Hematology, School of Medicine, Technical University Munich, D-81675 Munich, Germany. [2]Central Unit Electron Microscopy, German Cancer Research Center (DKFZ), D-69120 Heidelberg, Germany. [3]CECAD Research Center, Institute for Genetics, University of Cologne, D-50931 Cologne, Germany. [4]Walter Brendel Centre of Experimental Medicine, Ludwig-Maximilians-University Munich, 81377 Munich, Germany. [5]Department of Otorhinolaryngology, Ludwig-Maximilians-University Munich, 81377 Munich, Germany. [6]Institute of Immunology, University of Heidelberg, D-69120 Heidelberg, Germany. [7]Institute of Histology and Embryology, Medical University Innsbruck, A-6020 Innsbruck, Austria. [8]Center for Molecular Medicine (CMMC), University of Cologne, D-50931 Cologne, Germany. [9]Max-Planck Institute of Biochemistry, D-82152 Martinsried, Germany.

*Author for correspondence (m.moser@tum.de)

S.K., 0000-0003-4723-056X; M.M., 0000-0001-8825-5566

homeostasis and bone formation (Cao et al., 2020; Fu et al., 2020; Wu et al., 2015). Deletion of kindlin-2 in osteocytes and osteoblasts results in a striking osteopenia and mechanical defects in weight-bearing long bones, since impaired focal adhesion formation and defective cytoskeletal organization results in defective mechanotransduction (Cao et al., 2020; Fu et al., 2020; Qin et al., 2021).

In the current study, we investigated osteoclast function at very low kindlin-3 levels that still allow the formation of podosomes (Klapproth et al., 2019). We show that kindlin-3 hypomorphic osteoclasts are able to adhere to the bone matrix through formation of sealing zones in vitro and in vivo. However, these structures are leaky, leading to impaired bone resorption as they are unable to maintain high concentrations of proteinases, such as cathepsin K, in the resorption lacunae. Consequently, kindlin-3 hypomorphic mice develop mild osteopetrosis.

RESULTS
Kindlin-3 hypomorphic osteoclasts show impaired cell spreading, adhesion and signaling

Kindlin-3-deficient mice die shortly after birth, as they suffer from severe bleeding and leukocyte adhesion deficiency (Moser et al., 2009a, 2008). In contrast, kindlin-3 hypomorphic mice, which carry a neomycin resistance cassette within an intron of the *Fermt3* gene and therefore shows strongly reduced gene expression, are viable with a normal life expectancy, and are protected from spontaneous bleeding and infections (Klapproth et al., 2015). In order to study osteoclasts from kindlin-3 hypomorphic mice, we first determined their kindlin-3 expression levels. For this purpose, we differentiated bone marrow cells into osteoclast-like cells by adding macrophage colony-stimulating factor (M-CSF; also known as Csf1) and RANKL (also known as Tnfsf11) to the culture medium and determined their kindlin-3 levels by western blot analyses and densitometric measurements. In contrast, the kindlin-3-null cells used in this study were differentiated from fetal liver because it was not possible to isolate sufficient bone marrow cells from kindlin-3-knockout mice due to their early lethality and severe osteopetrosis. Similar to our previous results in platelets and neutrophils (Klapproth et al., 2015), the presence of a neomycin resistance cassette within one *Fermt3* allele (+/n) defined a hypomorphic allele, and reduced kindlin-3 protein expression to ~50%. The presence of two hypomorphic *Fermt3* alleles (n/n) or one hypomorphic and one *Fermt3*-null allele (n/−) lowered kindlin-3 expression in osteoclast-like cells to 10% and 5%, compared to wild-type cells, respectively (Fig. 1A,B) (Klapproth et al., 2015). We then determined the relative protein levels of kindlin-3, talin-1 and β-integrin subunits in wild-type macrophages and osteoclast-like cells compared to platelets, neutrophils and fibroblasts by mass spectrometry (Fig. S1). This relative quantification showed that macrophages and osteoclasts have a slightly higher ratio of talin-1 to kindlin-3 than platelets, neutrophils and fibroblasts (note that fibroblasts express kindlin-2; Fig. S1). Furthermore, the measurements confirmed that fibroblasts predominantly express β1 integrins, neutrophils β2 integrins and platelets β3 integrins, while osteoclast-like cells form all three integrin classes (Fig. S1). Taken together, these data suggest that kindlin-3 hypomorphic osteoclasts from n/− mice express more than 50 times less kindlin-3 than talin-1.

It is important to note that although kindlin-3-deficient osteoclast-like cells showed reduced adhesion and failed to spread into pancake-shaped polykaryons, their fusion and differentiation into multinucleated osteoclasts is hardly affected by the absence of kindlin-3 (Schmidt et al., 2011). To test the impact of low kindlin-3 levels on osteoclast adhesion and spreading in vitro, we generated osteoclast-like cells from the bone marrow of wild-type and kindlin-3 hypomorphic (n/n and n/−) mice using either low (20 ng/ml) or high (100 ng/ml) concentrations of M-CSF to trigger their differentiation and fusion into large polykaryons. Wild-type osteoclast-like cells started to reorganize their cytoskeleton and relocate their nuclei to the cell periphery within 4 days in culture. In contrast, kindlin-3 hypomorphic cells exhibited strongly delayed spreading but managed to form large, tartrate resistant acid phosphatase (TRAP)-positive, multinucleated and spread osteoclast-like cells 1 to 2 days later, depending on whether 10 or 5% of kindlin-3 protein was expressed (Fig. 1C). Notably, the delay in spreading could be only partially rescued by supplementing the medium with high concentrations of M-CSF. Of note, this concentration was sufficient to rescue spreading of integrin β3-deficient osteoclasts (Fig. 1D; Faccio et al., 2003). As signals originating from integrin adhesion sites control actin polymerization and cytoskeletal organization, we tested whether reduced adhesion signaling in kindlin-3 hypomorphic osteoclasts is responsible for the delay in cell spreading. Therefore, we generated pre-osteoclasts expressing different levels of kindlin-3 (+/+, n/n and n/−) by culturing bone marrow cells for only 2.5 days in M-CSF- and RANKL-containing medium, and plated them for 20 min on osteopontin, which is the major ligand of the principal osteoclast integrin αVβ3. With decreasing amounts of kindlin-3, we found a stepwise reduction in phosphorylation of Pyk2 and paxillin, two central signaling and adaptor proteins within the adhesion complex (Fig. 1E). In parallel, we tested pre-osteoclast adhesion on osteopontin, which also showed reduced cell adhesion at low kindlin-3 expression levels. Of note, the adhesion was significantly higher compared to kindlin-3-deficient pre-osteoclasts (Fig. 1F). Thus, we conclude that reduced integrin-mediated adhesion and signaling are responsible for the spreading defect of kindlin-3 hypomorphic osteoclasts.

To investigate whether other integrin classes are also functionally impaired at low kindlin-3 levels, we performed experiments with macrophages, which are related to and capable of differentiating into osteoclasts (Udagawa et al., 1990). Adhesion of hypomorphic (n/n and n/−) and kindlin-3-null macrophages to the β1 and αv integrin ligand fibronectin (Fig. S2A), the β2 integrin ligand ICAM-1 (Fig. S2B) and the α4β1 integrin ligand VCAM-1 (Fig. S2C) was reduced in a kindlin-3-dose-dependent manner. Adhesion to fibronectin and VCAM-1 was fully rescued in the presence of the exogenous integrin-activating agent Mn^{2+}, suggesting that a reduced number of active-ligand bound integrins account for the adhesion defect. In line with this, we detected reduced levels of active β1 integrins on the surface of kindlin-3 hypomorphic macrophages by flow cytometry using the activation-epitope specific antibody 9EG7 (Fig. S2D; Lenter et al., 1993). As a consequence of reduced integrin activity, hypomorphic macrophages showed diminished spreading on glass, cell-culture plastic and fibronectin-coated plastic (Fig. S2E–G). Importantly, the described defects in integrin function were not caused by altered integrin surface expression as shown by flow cytometry (Fig. S2H). Moreover, we tested the phagocytic activity of macrophages as a function of kindin-3 expression in vivo. In this model, recruitment of macrophages into the peritoneal cavity was induced by lipopolysaccharide (LPS) injection and phagocytic uptake of fluorescent beads was measured 6 h later by flow cytometry. While more macrophages, identified by F4/80, CD115 and CD11b-positive FACS staining, were collected from hypomorphic mice, uptake of fluorescent beads was significantly reduced (Fig. S2I,J).
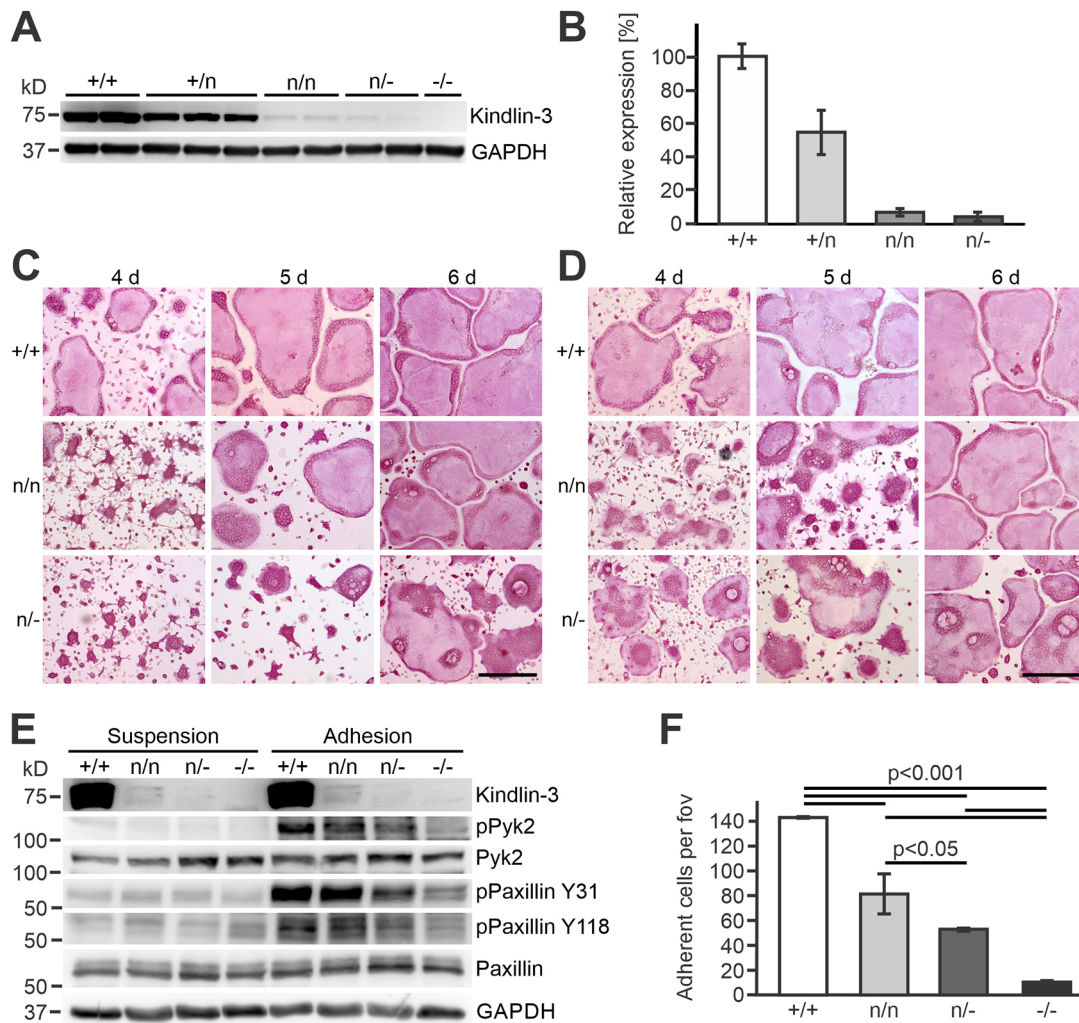
Fig. 1. Kindlin-3 hypomorphic osteoclasts are impaired in spreading and adhesion. (A,B) Western blot analysis of kindlin-3 in lysates from *in vitro* differentiated +/+, n/+, n/n, n/− and −/− osteoclast-like cells. GAPDH served as loading control. (B) Densitometric quantification of the kindlin-3 signal in A relative to the corresponding GAPDH signal. Mean±c.i.; n=5, 7, 5 and 5. (C,D) +/+, n/n and n/− bone marrow cells differentiated into osteoclast-like cells in response to 40 ng/ml RANKL and 20 ng/ml (C) or 100 ng/ml (D) M-CSF for 4–6 days and stained for TRAP activity. Scale bars: 200 µm. (E) +/+, n/n, n/− and −/− pre-osteoclasts were either kept in suspension or plated on a osteopontin coated surface for 20 min. Western blot analyses for kindlin-3, phosphorylated Pyk2, total Pyk2, phosphorylated paxillin Y31, phosphorylated paxillin Y118 and total paxillin. GAPDH served as loading control. (F) Static adhesion of +/+, n/n, n/− and −/− pre-osteoclasts to an osteopontin coated surface after 30 min. Values are given as mean±c.i.; n=3. fov, field of view. Images in C, D and western blot in E and are representative of three experiments. See Materials and Methods for details of statistical methods.

Taken together, low kindlin-3 expression in osteoclasts and macrophages results in reduced numbers of active integrins and impairs integrin-mediated adhesion and signaling.

Reduced kindlin-3 levels lead to changes in the morphology of podosomal adhesion structures

Macrophages and pre-osteoclasts arrange their podosomes into clusters, whereas mature, multi-nucleated osteoclasts arrange them into podosome belts at the cell periphery or more centrally located rings, also called sealing zones, depending on whether they are cultured on glass or on mineralized matrix, respectively (Georgess et al., 2014; Jurdic et al., 2006). Several studies have shown that kindlin-3 colocalizes with integrins and other plaque proteins to the podosomal ring structure in podosomes of macrophages and pre-osteoclasts (Klapproth et al., 2019; Schmidt et al., 2011). Accordingly, we found kindlin-3 in podosomal belts and sealing zones of mature osteoclast-like cells (Fig. S3A,B). Importantly, while the formation of mature podosomes requires kindlin-3,

expression of only 5% of kindlin-3 is already sufficient to recruit and assemble integrins and adaptor proteins in rings around the podosome actin core (Klapproth et al., 2019; Schmidt et al., 2011). Nevertheless, a strong reduction in kindlin-3 expression often resulted in the fragmentation of the podosome clusters into several smaller clusters and the actin cores were usually embedded in a more intense actin cloud (Fig. 2A). Moreover, the distribution of plaque proteins such as vinculin was more diffuse within the podosome clusters of hypomorphic cells (Fig. 2A–C). These abnormalities are also indicated by fluorescence intensity profiles through actin cores of podosome clusters of wild-type and hypomorphic cells. Here, control cells show a clear alternation of actin and vinculin, which becomes progressively lost at reduced kindlin-3 expression levels (Fig. 2B,C).

Next, we investigated whether these changes in podosome organization and cluster formation interferes with their rearrangement into podosome belts. Remarkably, kindlin-3 hypomorphic osteoclast-like cells were able to organize their
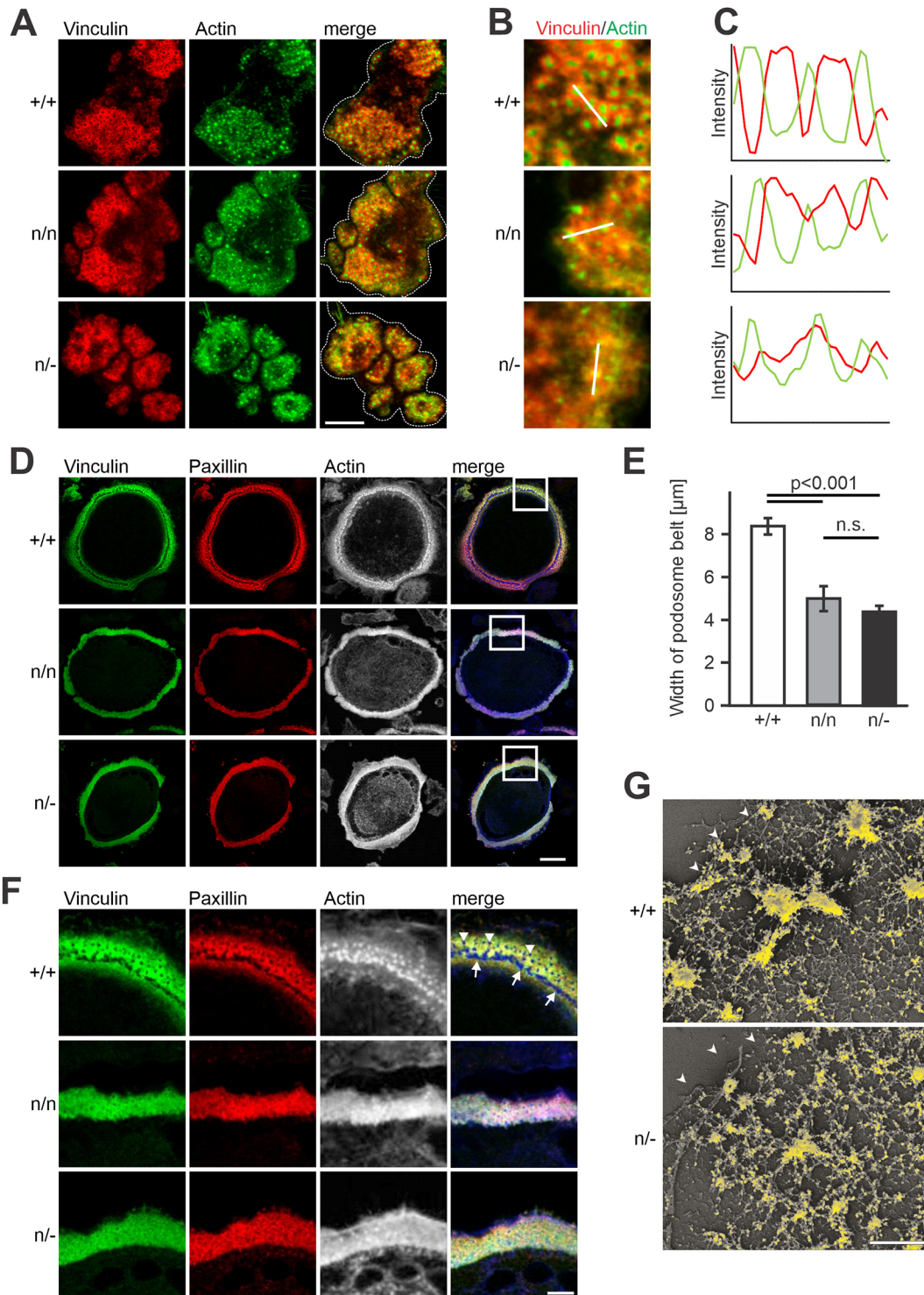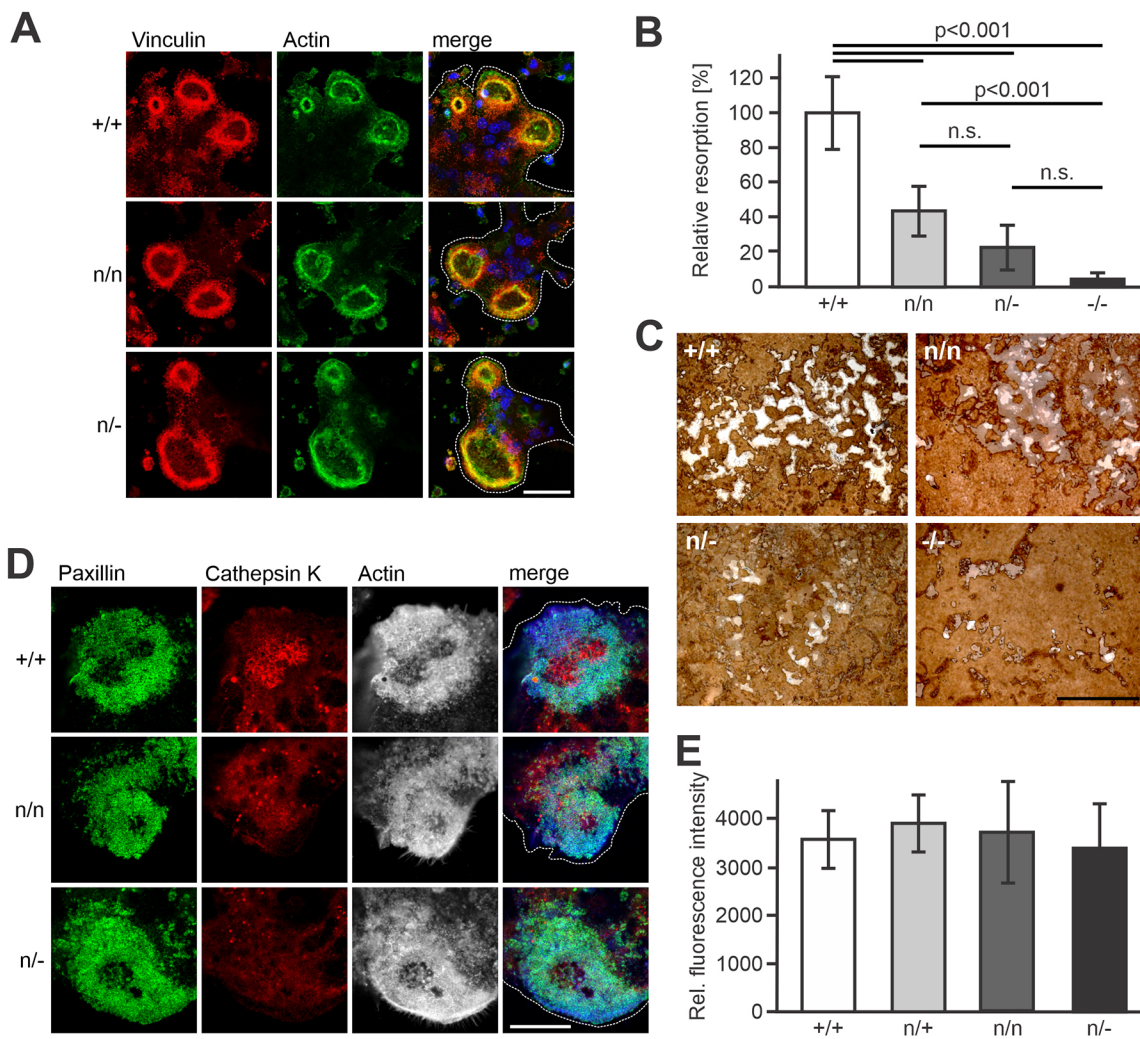
Fig. 2. Kindlin-3 hypomorphic (pre-)osteoclasts form podosomes and are able to arrange them into podosome belts. (A) Wild-type and hypomorphic pre-osteoclasts immunofluorescently labeled for vinculin (red) and F-actin (green) to visualize podosome clusters (dotted line marks cell edge). Scale bar: 10 µm. (B) Merged confocal images of podosomes labeled for vinculin (red) and actin (green). (C) Fluorescence intensity profile through three podosomes (indicated by the white lines in B) of +/+, n/n and n/− pre-osteoclasts. Length of white bars 4 µm. (D) Confocal images of wild-type and kindlin-3 hypomorphic osteoclast-like cells differentiated on glass coverslips and labeled for vinculin, (green), paxillin (red) and actin (white, in merge blue) to visualize podosome belt formation. Scale bar: 20 µm. (E) Width of podosome belts in mature osteoclast-like cells, measured on 60 cells from at least three different preparations. Values are given as mean±c.i. (F) Higher magnification of area in D indicated by white boxes. Arrowheads indicate podosomes cores; arrows point to the fused rim. Scale bar: 5 µm. (G) Scanning electron micrographs of actin immunogold (yellow) labeled ventral membrane preparations of +/+ and n/− osteoclast-like cells reveal the morphology of the peripheral podosome belt. Arrowheads mark the cell border. Scale bar: 1 µm. Images shown are representative of five (A–F) and two (G) experiments. See Materials and Methods for details of statistical methods; n.s., not significant.

podosomes in well-defined belts, that were, however, significantly thinner compared to those of wild-type cells (Fig. 2D,E). At higher magnification, distinct actin cores and an almost fused actin core ring are visible at the inner rim of wild-type podosome belts (Fig. 2F). The individual as well as the tightly associated actin cores are clearly devoid of the plaque proteins vinculin and paxillin, which colocalize with a less intense actin cloud. In strong contrast, individual actin cores can hardly be seen in podosome belts of kindlin-3 hypomorphic osteoclast-like cells and are embedded in an intense actin cloud, which colocalizes with a diffuse vinculin and paxillin signal (Fig. 2F). To gain further insights into the actin organization of the adhesion belts, we performed high-resolution scanning electron microscopy on ventral membrane preparations of wild-type and kindlin-3 hypomorphic osteoclast-like cells. In line with the immunofluorescence imaging results, actin cores of n/− cells were smaller than those of wild-type cells but were embedded in a denser mesh of actin filaments compared to controls, indicating that low kindlin-3 levels are not sufficient to organize the actin cytoskeleton within the adhesion belt (Fig. 2G; Fig. S3C,D).

Sealing zones from kindlin-3 hypomorphic osteoclasts are functionally impaired

We then tested the ability of kindlin-3 hypomorphic osteoclasts to form sealing zones. To this end osteoclast-like cells were cultured on a calcified, bone-like matrix. Despite their low kindlin-3 expression, kindlin-3 hypomorphic osteoclast-like cells also assembled sealing zones that seemed indistinguishable from those of control cells (Fig. 3A). In order to measure the resorptive capacity of kindlin-3 hypomorphic osteoclast-like cells *in vitro*, we cultured them on a calcified matrix and determined the resorbed area. Whereas osteoclast-like cells differentiated from kindlin-3 deficient fetal liver cells hardly resorb any matrix due to their impaired adhesion and spreading (Schmidt et al., 2011), kindlin-3 hypomorphic osteoclast-like cells also exhibited a progressive reduction in their resorptive activity, which is concordant with the decrease in kindlin-3 levels (Fig. 3B,C).

Sealing zones tightly attach and seal the ventral plasma membrane of the osteoclast to the underlying bone and encase a special membrane compartment, called the ruffled border. Within

Fig. 3. Sealing zone assembly is maintained in kindlin-3 hypomorphic osteoclast-like cells but their function is affected. (A) Wild-type and hypomorphic osteoclast-like cells differentiated on mineralized matrix immunofluorescently labeled for vinculin (red) and actin (green) to visualize sealing zone formation. Scale bar: 20 µm. (B,C) Quantification of the resorption activity of +/+, n/n, n/− and −/− osteoclast-like cells cultured on calcium phosphates coated slides. Scale bar: 200 µm. Values are given as mean±c.i.; $n=6$. (D) Wild-type and hypomorphic osteoclast-like cells plated on mineralized matrix labeled for vinculin (green), cathepsin K (green) and actin (white, in merge blue). Dotted line indicates cell edge. Scale bar: 10 µm. (E) Cathepsin K activity assay on lysates of *in vitro* differentiated +/+, +/n, n/n and n/− osteoclast-like cells. Values are given as mean±c.i.; $n=3, 4, 4$ and 3. Images shown are representative of three (A,D) and six (C) experiments. See Materials and Methods for details of statistical methods; n.s., not significant.

this compartment, locally secreted protons and proteinases degrade the mineral and organic components of the bone matrix. One of these proteinases is cathepsin K, which is secreted in large amounts at the ruffled border and accumulates in the resorption lacunae to cleave key bone matrix proteins such as collagen I (Saftig et al., 2000). We analyzed accumulation of cathepsin K at the ventral cell membrane by confocal microscopy, where it was enriched in sealing zone encircled areas of control osteoclast-like cells. In strong contrast, cathepsin K was not found to be accumulated at the ventral cell membrane of kindlin-3 hypomorphic osteoclast-like cells (Fig. 3D). Given that cathepsin K activity in cell lysates of wild-type and hypomorphic osteoclast-like cells was similar (Fig. 3E), we assume that the adhesion structures of hypomorphic cells are not tight enough to prevent leakage of the secreted proteinases from the resorption area.

Kindlin-3 hypomorphic mice develop a mild osteopetrosis

To investigate whether the reduced resorptive activity of kindlin-3 hypomorphic osteoclasts causes an osteopetrotic phenotype in mice, we analyzed tibiae of control and kindlin-3 hypomorphic mice by means of histology and peripheral quantitative computer tomography (pQCT). Hematoxylin and Eosin (H&E) staining of paraffin sections and Masson–Goldner staining of sections of PMMA-embedded bones, which stains the bone matrix, suggested increased trabecular bone in 4.5-month-old kindlin-3 hypomorphic mice (Fig. 4A,B). An increase in trabecular bone mineral density (BMD), as measured by pQCT of bones from 6-month-old mice confirmed these findings (Fig. 4C). Heterozygous mice, which express ∼50% of wild-type kindlin-3 levels, appeared normal. Notably, kindlin-3 hypomorphic mice remained osteopetrotic throughout life, as the difference in trabecular BMD between control and hypomorphic mice was still present at the age of 2 years (Fig. 4D).

Next, we determined the number and location of osteoclasts on bone sections. TRAP staining and histomorphometric analysis of bones of 6-month-old mice revealed more than twofold and threefold elevated osteoclast numbers per bone surface in n/n and n/− mice, respectively (Fig. 4E,F). The eroded surface, which represents the bone surface area covered by osteoclasts, was also increased (Fig. 4G). Interestingly, both the absolute number of TRAP-positive osteoclasts normalized to the bone surface area, as well as the fraction of bone surface covered by osteoclasts was significantly increased in kindlin-3 hypomorphic mice.

To further corroborate the hypothesis that the resorption defect results from leaky sealing zones, we performed transmission electron microscopy (TEM) on ultrasections of the tibia of 7-day-old wild-type and n/− mice. These studies revealed that kindlin-3 hypomorphic osteoclasts, like osteoclasts from control mice, attach to the bone surface, are polarized showing extensively folded membrane structures of the ruffled border and are able to generate resorption lacunae (Fig. 4H). Sealing zones from wild-type osteoclasts, however, were clearly separated from the ruffled border and the cytoplasm (Fig. 4H, indicated by white arrowheads) and appeared as homogeneous patches that were devoid of cell organelles and lie smoothly on the bone surface (Fig. 4H; Fig. S4A, indicated by black arrows). In stark contrast, in kindlin-3 hypomorphic osteoclasts, no clear separation between the ruffled border and the sealing zone was apparent, in particular the folded ventral plasma membrane of the ruffled border extended into the sealing zone thereby preventing close contact with the bone surface (Fig. 4H; Fig. S4A, indicated by white arrows). Furthermore, the sealing zones of kindlin-3-hypomorphic osteoclasts often contained

vesicles and were not clearly separated from the rest of the cytoplasm. In line with the reduced resorptive activity, we found intact collagen fibers in the resorption lacunae and between membrane folds of the ruffled border of kindlin-3 hypomorphic osteoclasts pointing towards insufficient resorptive activity (Fig. 4I), which might also be caused by structural defects of the ruffled border. While the ruffled border in control cells comprises an array of lamellar pillars, it appeared as a sponge-like structure in hypomorphic osteoclasts (Fig. 4H; Fig. S4B). In cross sections, the ruffled border of hypomorphic osteoclasts appeared as a laterally fused network rather than a cluster of individual lamella (Fig. S4C). Strikingly, adjacent to the ruffled border, hypomorphic cells usually contained many large cytoplasmic vesicles (Fig. 4H; Fig. S4B). Thus, these ultrastructural analyses indicate that reduced bone resorption in kindlin-3 hypomorphic mice is primarily due to structural defects in the sealing zone and the ruffled border of their osteoclasts.

DISCUSSION

In the present study, we wanted to investigate the effect of low kindlin-3 expression on hematopoietic cells, whose integrin-mediated functions are not immediately dependent on rapid integrin activation and ligand binding. Therefore, we chose also osteoclasts as a model for the following reasons. Firstly, their fusion and differentiation take place in the bone marrow and they do not require integrin-dependent homing processes to reach their destination. Secondly, their fusion into polykaryons and differentiation are independent of kindlin-3-mediated integrin activity (Schmidt et al., 2011). Finally, in contrast to platelets and neutrophils, osteoclasts form defined highly complex integrin-mediated adhesion structures.

Our studies confirmed a number of findings already obtained on kindlin-3 hypomorphic platelets and neutrophils. A stepwise reduction of kindlin-3 expression in osteoclasts, as well as in macrophages, results in a progressive reduction in cell adhesion and cell spreading, which is due to a reduced number of activated integrins and reduced integrin-mediated signaling. In this context, it is necessary to mention that reduced adhesive properties are most likely the reason for the increased number of macrophages flushed from the peritoneal cavity. Indeed, kindlin-3 hypomorphic macrophages exhibit clearly reduced phagocytic activity. It is remarkable that even 5% of kindlin-3 and thus a shift in the ratio of kindlin-3 to talin-1 of at least 1 to 50 is sufficient to allow attachment of osteoclasts to the bone surface and induce cell spreading and polarization, which is not possible in the absence of kindlin-3. In other words, even minimal levels of kindlin-3 are sufficient to trigger integrin-dependent cell functions.

A key difference between osteoclasts that do not produce kindlin-3 and those that produce only 5% kindlin-3 is that the latter cells are able to adhere to the bone matrix and form resorption structures. In stark contrast, kindlin-3-knockout osteoclasts float within the bone marrow cavity and, despite their greatly increased numbers, only a few are detected at the bone surface. Consequently, the eroded surface, which is the bone surface area that is covered by osteoclasts, is strongly decreased in kindlin-3 deficient mice (Schmidt et al., 2011), while it is increased in kindlin-3 hypomorphic mice, because weak or even kindlin-3-independent adhesion may be possible at high ligand density or when only weak shear forces act on the cells (Moretti et al., 2018, 2013). By contrast, histological studies of bone sections revealed that kindlin-3 hypomorphic osteoclasts bind efficiently to the bone surface, although they showed a strong adhesion defect in *in vitro* adhesion assays. This may be mainly due
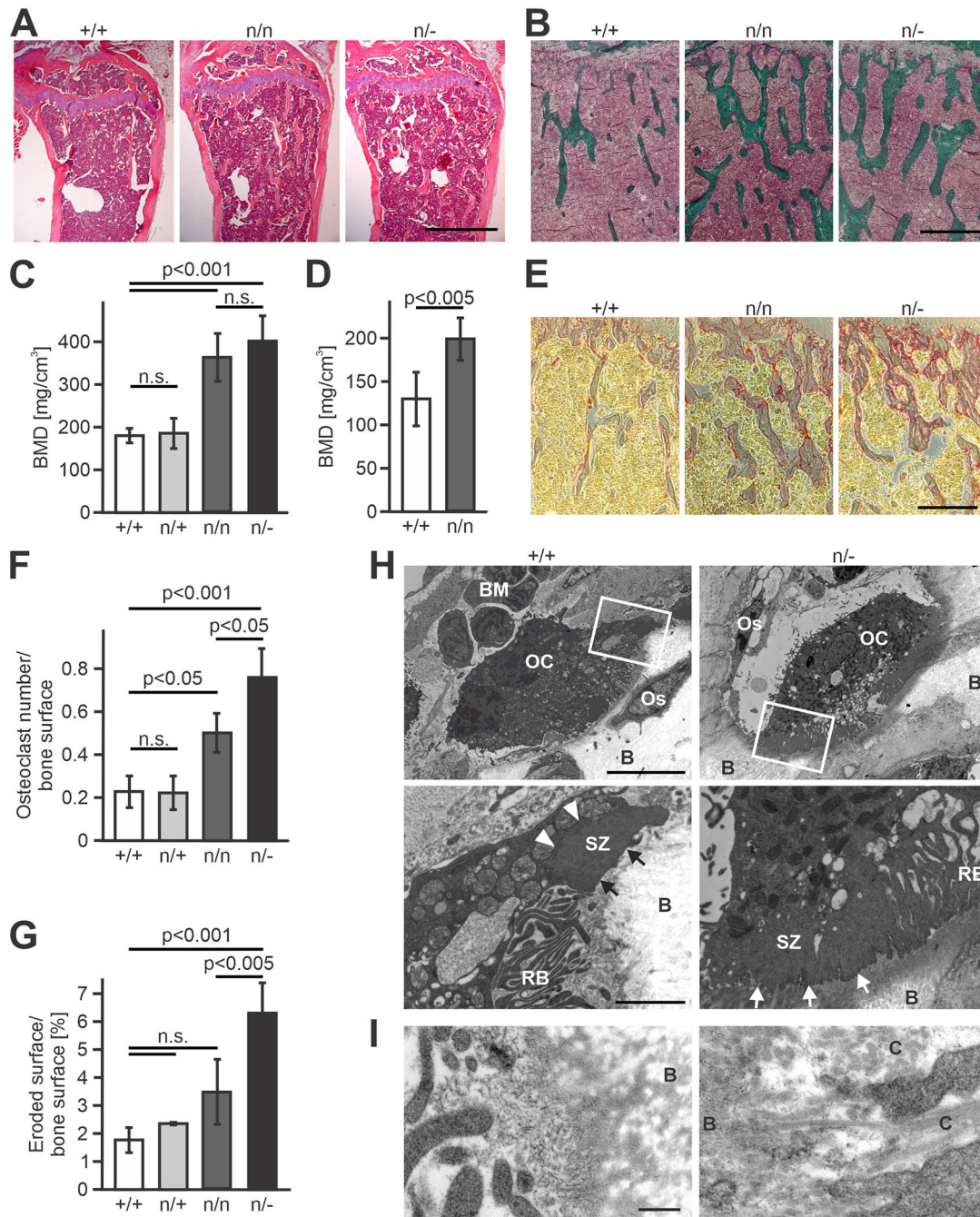
Fig. 4. Kindlin-3 hypomorphic mice suffer from mild osteopetrosis. (A,B) Histological sections of the tibiae of 4.5-month-old +/+, n/n and n/− mice stained with H&E (A) and according to the Masson–Goldner protocol (B). Scale bars: 1 mm (A); 200 µm (B). (C,D) Bone mineral density from bones of mice aged 6 (C) and 24 (D) months as assessed by quantitative peripheral computer tomography. Values are given as mean±s.d.; n=8, 3, 4 and 5 (C), and n=5, 5 (D). (E) Histological sections of the tibiae of 4.5-month-old +/+, n/n and n/− mice stained for TRAP activity. Scale bar: 200 µm. (F) Histomorphometric analyses of the number of osteoclasts relative to the bone surface in +/+, n/+, n/n and n/− mice at the age of 6 months. Values are given as mean±s.d.; n=5, 2, 3 and 5. (G) Histomorphometric analyses of the bone surface directly covered by osteoclasts relative to the total bone surface in +/+, n/+, n/n and n/− mice at the age of 6 month. Values are given as mean±s.d.; n=5, 2, 3 and 5. (H,I) Electron microscopy on bone ultrasections in +/+ and n/− mice at postnatal age of 7 days. Scale bars: 10 µm (H, top), 2.5 µm (H, bottom), 250 nm (I). OC, osteoclast; Os, osteocyte; B, bone; BM, bone marrow; SZ, sealing zone; RB, ruffled border; C, Collagen. Arrows indicate contact area between sealing zones and bone surface. White arrowheads indicate the discrete border between the sealing zone and cytoplasm in wild-type osteoclasts. Images shown are representative of three mice. See Materials and Methods for details of statistical methods; n.s., not significant.

to the fact that these cells are only exposed to very low shear forces within the bone marrow cavity, in contrast to circulating neutrophils or platelets, which have to adhere to the vascular endothelium.

Kindlin-3-knockout animals already show massive osteopetrosis at birth. It is therefore all the more surprising that animals that have only 5% of the usual level of kindlin-3 only develop a mild osteopetrosis that does not worsen over time. The rather mild bone phenotype is probably owing to three reasons. First, in addition to their ability to adhere, kindlin-3 hypomorphic mice compensate for the impaired osteoclast function partly by increasing their numbers compared to control animals, which is certainly due to their reduced

ability to resorb bone and thereby release calcium ions. As we have already shown for kindlin-3-knockout mice, impaired bone resorption leads to decreased blood Ca^{2+} level, which triggers increased release of parathyroid hormone (PTH) by the parathyroid gland. PTH in turn induces the release of RANKL from osteoblasts, strongly promoting osteoclast differentiation (Schmidt et al., 2011). Second, the strongly elevated osteoclast numbers in kindlin-3 hypomorphic and knockout mice suggests that differentiation and fusion of osteoclasts *in vivo* can occur independently of integrin-mediated adhesion, especially at high precursor density. Third, kindlin-3 hypomorphic osteoclasts can at least to a certain extent degrade the bone matrix. The latter is evidenced not only by *in vitro* resorption assays but also by TEM of ultrathin bone sections showing polarized kindlin-3 hypomorphic osteoclasts that have formed a ruffled border framed by a sealing zone on top of resorption bays and the presence of degraded material in intracellular vesicles.

Although only 5% kindlin-3 is sufficient for formation of adhesion belts or sealing zones, our cell biological studies revealed deficits in these adhesion structures, which explains the adhesion defect. Most obvious are the formation of thinner podosome belts by kindlin-3 hypomorphic osteoclast-like cells cultured on glass, in which the podosomes are embedded in a diffuse actin cloud and in which the actin cores are less clearly separated from the surrounding ring of integrins and adaptor proteins. This indicates that kindlin-3 is not only critically involved in integrin activation but also in the assembly and organization of the adhesion structures. Consistent with this, we have recently shown that kindlin-3 regulates the turnover of podosomes by recruiting leupaxin to the adhesion site that controls paxillin phosphorylation via the phosphatase PTP-PEST (also known as Ptpn12) (Klapproth et al., 2019). Furthermore, direct interactions of kindlins with actin, paxillin and ILK have been demonstrated, indicating a central role of kindlins in the organization of the cytoskeleton (Bledzka et al., 2016; Bottcher et al., 2017; Gao et al., 2017; Huet-Calderwood et al., 2014; Theodosiou et al., 2016). The diffuse actin network, as well as the reduced diameter of actin cores of podosomes, also seen in electron microscopy studies, clearly support this. Moreover, our ultrastructural analyses revealed striking differences in the ruffled border, suggesting that the generation of a resorptive milieu by the ruffled border is additionally impaired in kindlin-3 hypomorphic osteoclasts due to the described defects in integrin signaling and cytoskeletal organization.

How kindlin-3 regulates the actin cytoskeleton within this context, remains to be further elucidated. The reduced number of active integrins and the impaired adhesion structure assembly in kindlin-3 hypomorphic cells results in a weaker linkage between the extracellular matrix and the actin cytoskeleton, which affects its maturation. Beside the indirect connection of kindlin-3 to actin, for example, via ILK or paxillin (Bottcher et al., 2017; Fukuda et al., 2014; Gao et al., 2017; Huet-Calderwood et al., 2014; Theodosiou et al., 2016), regulation of several signaling molecules involved in actin cytoskeletal organization, such as Pyk2, Syk, Vav1 and RACK1, depend on the presence of kindlin-3 (Feng et al., 2012; Klapproth et al., 2019; Schmidt et al., 2011; Xue et al., 2013).

In sum, the kindlin-3-knockout and hypomorphic mouse models allowed us to unravel different aspects of the role of kindlin-3 in regulating osteoclast-mediated bone resorption. Whereas studies on kindlin-3-knockout animals showed that osteoclast differentiation and fusion, as well as osteoblast function, are not significantly altered in the absence of kindlin-3, spreading and formation of complex integrin-mediated adhesion structures, such as adhesion

belts or sealing zones, are completely abolished. Thus, these cells hardly adhere to the bone surface but predominantly float in the bone marrow cavity, which leads to to massive osteopetrosis being already present at birth (Schmidt et al., 2011). In contrast, minimal amounts of kindlin-3 are sufficient to attach osteoclasts to the bone surface and induce cell spreading and polarization. Importantly, in our study using kindlin-3 hypomorphic mice, we demonstrated that kindlin-3 is also a key organizer of the integrin adhesion complex. Moreover, whereas the cause of osteopetrosis is usually either defective maturation of osteoclasts or impaired generation of an acidic milieu and secretion of proteinases, our study shows that structural problems in the organization of integrin adhesion structures of osteoclasts can also result in osteopetrosis.

MATERIALS AND METHODS

Mice
Kindlin-3-deficient (−/−) and kindlin-3 hypomorphic (+/n; n/n; n/−) mice were described previously (Klapproth et al., 2015; Moser et al., 2008). Mouse experiments were performed with the approval of the District Government of Bavaria, Germany.

Reagents
Recombinant murine mouse-colony stimulating factor (M-CSF) and receptor activator of NF-κB ligand (RANKL) were obtained from Peprotech (Hamburg, Germany).

Antibodies
The following antibodies were used for immunofluorescent labeling of cells: mouse anti-vinculin antibody (Sigma-Aldrich, Deisenhofen, Germany); mouse anti-cathepsin K (Calbiochem, Darmstadt, Germany); rabbit anti-paxillin (Abcam, Cambridge, UK); mouse anti-talin (Sigma-Aldrich). Phalloidin dyes and secondary antibodies were obtained from Invitrogen (Darmstadt, Germany).

The following antibodies were used for flow cytometry: hamster IgG anti-integrin β1-PE, isotype control hamster IgG-PE (both from Biolegend, San Diego, USA); rat IgG2a anti-integrin β2, rat IgG2a anti-integrin α4, rat IgG2a anti-integrin α5, rat IgG2a anti-integrin αL, rat IgG1 anti-integrin αV, isotype control rat IgG1, isotype control rat IgG2a, rat anti-integrin β1 clone 9EG7 (all from BD Biosciences); hamster IgG anti-integrin β3, rat IgG2b anti-integrin αM, isotype control rat IgG2b (all from eBioscience, Frankfurt am Main, Germany).

The following antibodies were used for western blotting: mouse anti–glyceraldehyde 3-phosphate dehydrogenase (anti-GAPDH; Merck, Darmstadt, Germany); rabbit anti-Pyk2, rabbit anti-pPyk2 Tyr402, (both from Cell Signaling Technology, Leiden, Netherlands); rabbit anti-paxillin (Abcam); rabbit anti-paxillin Y31; rabbit anti-paxillin Y118 (both from Thermo Fisher Scientific, Darmstadt, Germany); rabbit anti-kindlin-3 antibody is made in house (Ussar et al., 2006). HRP-labeled secondary antibodies were purchased from Jackson ImmunoResearch Laboratories (Suffolk, UK). Catalog numbers and antibody dilutions are provided in Table S1.

Cell culture
Bone marrow-derived macrophages (BMDMs) were generated by treating bone marrow cells with R10 medium [RPMI 1640 containing 10% fetal calf serum (FCS), 25 mM HEPES, 100 U/ml penicillin, 100 µg/ml streptomycin, 2 mM L-Glu, 50 µM β-mercaptoethanol] supplemented with M-CSF for 6 days. Kindlin-3$^{−/−}$ macrophages were differentiated from fetal liver cells accordingly.

Osteoclast-like cells were also differentiated from bone marrow or fetal liver cells. The cells were kept in α-MEM supplemented with 20 ng/ml M-CSF overnight and nonadherent cells were collected after 24 h. Leukocytes were isolated from the interface after centrifugation at 1000 *g* for 20 min in leukocyte separation medium (Laboratoires Eurobio, Les Ulis, France), then washed with α-MEM medium and seeded at a concentration of 2000 cells/mm^2 in osteoclast differentiation medium [α-MEM containing

10% FCS, 100 U/ml penicillin, 100 µg/ml streptomycin and supplemented with 60 ng/ml M-CSF (unless stated otherwise) and 40 ng/ml RANKL]. Cells were cultured at 37°C in 5% CO_2 for 5–8 days, and medium was changed every second day. Staining for TRAP activity was performed after 4–6 days in culture. Pictures were taken with a microscope (Axioskop; Carl Zeiss, Inc., Oberkochen, Germany) equipped with a DC500 camera (Leica), using a 20× NA 0.50 objective and IM50 software. Pictures were edited with Photoshop (Adobe).

For pre-osteoclast generation, 5×10^6 interface cells were plated on a 10-cm dish and cultured in osteoclast differentiation medium for 3 day. Cells were washed with PBS and lifted with 0.1% Trypsin-EDTA.

Cell culture medium and supplements were purchased from Gibco, Invitrogen, Thermo Fisher Scientific, unless otherwise stated.

Immunofluorescence microscopy
BMDM and (pre-)osteoclasts were immunofluorescently labeled as previously described (Schmidt et al., 2011). Cells were plated on 12-mm coverslips or osteologic slides (BD Biosciences) and fixed with 4% paraformaldehyde (PFA) in PBS for 10 min. Permeabilization and blocking was performed with 0.1% Triton X-100 and 1.5% bovine serum albumin (BSA) in PBS for 1 h. Cells were then incubated with the primary antibody in 1% BSA for 3 h at room temperature or at 4°C overnight. F-actin was visualized with Alexa Fluor 488–phalloidin or Alexa Fluor 647–phalloidin.

Cells were imaged at room temperature with a Leica TCS SP5 X confocal microscope (Leica, Bonn, Germany) using 63×NA 1.40 oil objective lenses and Leica Confocal Software (LAS AF). Single channels were imaged sequentially. All pictures were processed with Photoshop (Adobe Systems, San José, California, USA).

The podosome belt width was obtained by measuring the thickness of the vinculin ring of at least 20 belts from osteoclast-like cells that were differentiated in three or more independent preparations.

Histology
Long bones of 4.5-month-old mice were dissected, freed from soft tissue, decalcified in 10% EDTA in PBS for 2 weeks and embedded in paraffin. Paraffin sections were stained with H&E and for TRAP activity using a commercial kit (Sigma-Aldrich). For Masson–Goldner staining bones were fixed in 70% ethanol and embedded in polymethylmethacrylate. 3-µm sections of the distal femur were deplasticized and stained for Masson-Goldner with hematoxylin (Gill II; Carl Roth, Karlsruhe, Germany), acid Fuchsin-Ponceau Xylidine, and phosphomolybdic acid-Orange G for visualizing cells, and osteoid and Light Green for visualizing mineralized matrix.

Pictures were taken by bright field microscopy with a microscope (Axioskop; Carl Zeiss, Inc.) equipped with a DC500 camera (Leica), 10× NA 0.3 and 20× NA 0.50 objectives, and IM50 software. Pictures were edited with Photoshop (Adobe).

Bone mineral density and histomorphometric measurements
pQCT of the distal femur was performed with XCT Research SA⁺ (StraTec Medizintechnik). Total and trabecular bone mineral density (BMD) was measured by QCT of the distal femur (XCT Research SA-StraTec) at 7.5% of the bone length below the growth plate of the femur using peel-mode 2.

Histomorphometric analysis was performed according to the standards set forth by the American Society for Bone and Mineral Research as described previously (Bentmann et al., 2010). The following parameters were examined: bone surface, osteoclast number and osteoclast surface. Measurements were performed by a person who was blind to the genotype of the mice.

Electron microscopy
For TEM, freshly excised tibia from mice killed at 7 days old, were resin-embedded, without decalcification, according to standard procedures [immersion-fixation in cacodylate-buffered (100 mM, pH 7) 4% formaldehyde and 1% glutaraldehyde, post-fixation in 1% osmium tetroxide, en-bloc staining with 1% uranylacetate, graded dehydration with ethanol and embedding in epoxide (glycidether, NMA, DDSA, Serva,

Heidelberg, Germany)]. Ultrathin sections at nominal thickness of 60 nm and contrast-stained with lead-citrate and uranylacetate were observed in a Zeiss EM 910 at 100 kV (Carl Zeiss). Micrographs were taken on image-plates scanned at 15 µm resolution (Ditabis, Pforzheim, Germany).

Primary osteoclast-like cells were differentiated on glass coverslips and 'unroofed' as described previously (Heuser, 2000; Luxenburg et al., 2007; Schmidt et al., 2011). Briefly, cells were treated with hypotonic buffer (20% PHEM buffer; 6 mM PIPES, 5 mM HEPES, 0.4 mM Mg_2SO_4, and 2 mM EGTA, pH 6.9) and opened by sonication for 2 s. The resulting ventral membrane preparations were fixed with 4% formaldehyde in 0.1 M phosphate buffer (pH 7.4, 1 h at room temperature) and subjected to indirect immunogold labeling essentially as described previously (Luxenburg et al., 2007). Antibodies were mouse anti-actin (Chemicon MAB1501R; 1:500) and goat anti-mouse-IgG coupled to 5 nm colloidal gold, followed by silver enhancement (Nanoprobes HQ silver). Samples were briefly postfixed with 0.5% (w/v) aqueous OsO_4, dehydrated, critical-point dried and sputter-coated with 2 nm platinum. Samples were viewed with a field emission scanning electron microscope (DSM 982-Gemini; Carl Zeiss, Inc.) equipped with secondary electron (SE) and backscattered secondary electron (BSE) detectors at 10 kV. The fine structure of podosomes was documented by using a conventional SE detector; low magnification overviews of ventral plasma membranes required high-contrast imaging with an in-lens detector. BSE imaging was used to map immunogold-silver distribution. Optionally, signals of the SE and BSE detector were mixed by using the signal mixer of the microscope. Pseudocolouring was performed with algorithms in Adobe Photoshop CS6.

Adhesion assays
Adhesion assays were performed as described previously (Chavakis et al., 2008; Schmidt et al., 2011). Non-cell-culture treated 96-well plates (Falcon, BD Biosciences) were coated with 4 µg/ml recombinant human intercellular adhesion molecule-1 (ICAM-1) and recombinant human vascular cell adhesion molecule-1 each (VCAM-1), 2 µg/ml osteopontin (all from R&D Systems) or 5 µg/ml bovine plasma fibronectin (Merck-Millipore) in coating buffer (20 mM Tris-HCl pH 9.0, 150 mM NaCl, 2 mM $MgCl_2$) overnight at 4°C. The wells were blocked for 1 h at room temperature with 1.5% BSA in PBS.

5×10^4 macrophages or pre-osteoclasts in RPMI 1640, 0.1% FCS and 25 mM HEPES pH 7.4 (Gibco, Thermo Fisher Scientific) with or without 1 mM $MnCl_2$ were seeded on indicated ligands for 30 min at 37°C, washed twice with PBS and fixed with 4% PFA in PBS for 15 min. Each experiment was performed in quadruplets. After fixation, adherent macrophages were stained with 5 mg/ml Crystal Violet in 2% ethanol for 30 min, washed and the remaining dye was dissolved in 2% SDS and the staining intensity was measured in an ELISA plate reader at 595 nm. The number of adherent pre-osteoclasts was determined by acquisition of three phase contrast pictures from each well and counting adherent cells.

To visualize cell spreading, cells were seeded for 2 hours on different surfaces, fixed with 4% PFA in PBS for 15 min, imaged with an Axiovert 40C microscope (Zeiss) equipped with a 20× NA 0.3 objective (Zeiss).

Adhesion signaling
Bone marrow derived pre-osteoclasts were trypsinized and kept in serum-free α-MEM in suspension for 1.5 h at 37°C. Then cells were either kept in suspension or plated on a surface coated with 2 µg/ml osteopontin for 20 min. Cells were carefully washed with ice cold PBS and lysed in Tris-buffered saline (TBS), containing 1% Triton X-100, protease inhibitors (Roche, Penzberg, Germany) and phosphatase inhibitor cocktails (Sigma-Aldrich); 40 µg of lysates were subjected to 10% SDS-PAGE and subsequent western blot analyses.

Resorption assay
Osteoclast-like cells differentiated in vitro from bone marrow cells were plated in osteoclast differentiation medium on Biocoat™ Osteologic™ slides coated with bone biomaterial (BD Biosciences) for 1 week. To quantify matrix resorption, cells were removed from the slides by treating them with 1% Triton X-100 and mechanical agitation. Pictures were

obtained with a microscope (Axioskop; 20× NA 0.50 objective), and the resorbed area was quantified using MetaMorph software (Molecular Devices, LLC., San Jose, CA, USA).

Cathepsin K activity assay

Functional cathepsin K concentration was measured in protein lysates of cultured osteoclast-like cells using a Cathepsin K Activity Assay kit (BioVision, Inc., Milpitas, USA). The assay was performed according to the manufacturer's instructions using 50 µg protein lysate per measurement.

Flow cytometry

Cells were incubated with Fc receptor-blocking antibody (Merck-Millipore) in FACS buffer (PBS with 1% FCS and 2 mM Na_2EDTA) and then stained with appropriate fluorophore-conjugated monoclonal antibodies for 30 min on ice. Analysis was performed with a FACSCalibur, a FACSAria or a FACSCanto (BD Biosciences) and data were analyzed using FlowJo software.

Measurement of 9EG7 binding

BMDMs were treated with Fc receptor-blocking antibody for 10 min. The cells were kept either unstimulated or activated with 2 mM Mn^{2+} and incubated with Alexa Fluor 647-conjugated anti-CD29 antibody (clone 9EG7, BD Biosciences) for 30 min at 37°C. Antibody labeling was performed using an Alexa Fluor 647 antibody labeling kit from Invitrogen according to the manufacturer's protocol. Cells were analyzed using a FACSAria.

Peritoneal leukocyte trafficking and phagocytosis assay

Peritoneal inflammation was induced by intraperitoneal stimulation with 1 µg TNF-α (R&D Systems) in 350 µl PBS. After 4 h, 200 µl of pHrodo Green E coli BioParticles Conjugate (2 mg/ml; Thermo Fisher Scientific) was administered by intraperitoneal (i.p.) injection. Mice were killed 2 h later and their peritoneal cavity was washed with 10 ml of ice-cold PBS. The total number of leukocytes in the peritoneal lavage fluid was measured using the ProCyte Hematology analyzer (IDEXX, Westbrook, Maine, USA). Subsequently, FACS stainings were performed using antibodies directed against CD45 (APC/Cy7, Biolegend), CD11b (PerCP-Cy5.5, eBioscience/ Thermo Fisher), Gr-1 (PE, eBioscience), CD115 (APC, Biolegend), F4/80 (eFluor 450, eBioscience). After erythrocyte lysis (1:10, BD FACS Lysing solution, BD Biosciences), samples were washed and analyzed by flow cytometry.

MS-based proteome analysis

Samples for mass spectrometry (MS) analysis were prepared by in-solution digestion. Tissues were lysed in 4% SDS in PBS, heated to 95°C and sonicated. 20 µg of protein were precipitated overnight in 4 volumes (v/v) of ice-cold acetone. Protein pellets were extracted by centrifugation at 13,000 g for 10 min and dissolved in urea buffer (6 M Urea, 2 M Thiourea in 10 mM HEPES, pH 8.0). Urea-containing samples were reduced by applying DTT at a final concentration of 5 mM for 1 h at room temperature, alkylated with a final concentration of 40 mM 2-iodoacetamide (IAA) for 30 min in the dark at room temperature, digested with 1 µl LysC for 2–3 h at room temperature, diluted with 50 mM ammonium bicarbonate to a urea concentration of 2 M, incubated with 1 µl 0.5 mg/ml trypsin overnight at room temperature, acidified to 1% formic acid and purified using Stop and Go extraction tips (StageTips) (Rappsilber et al., 2003).

Proteome samples were analyzed using a liquid chromatography tandem mass spectrometry on a Q-Exactive™ HF-X Hybrid Quadrupole-Orbitrap™ (Thermo Fisher Scientific). Chromatographic peptide separation was achieved on PoroShell 120 packed 50 cm analytical columns coupled to an EASY-nLC 1000 HPLC system and a binary buffer system consisting of buffer A (0.1% formic acid) and buffer B (80% acetonitrile and 0.1% formic acid). Samples derived from in-solution digestion were measured over a 90 min gradient, raising the content of buffer B from 4% to 23% over 65 min, from 23% to 55% over 13 min and from 55% to 95% over 3 min. The column was washed with 95% buffer B for 9 min. Full MS spectra (350–1650 m/z) were recorded at a resolution (R) of 60,000, maximum injection time (max. IT) of 20 ms and automatic gain control (AGC) target

of 3×10^6. The 22 most abundant ion peptides in each full MS scan were selected for HCD fragmentation at nominal collisional energy (NCE) of 28. MS2 spectra were recorded at R=15,000, a maximum IT of 22 ms, and an AGC target of 1×10^5.

The generated MS raw data were analyzed using MaxQuant analysis software and the implemented Andromeda software (1.5.3.8) (Cox and Mann, 2008; Cox et al., 2011). Peptides and proteins were identified using the mouse UniProt database with common contaminants. All parameters in MaxQuant were set to the default values. Trypsin was selected as the digestion enzyme, and a maximum of two missed cleavages was allowed.

Methionine oxidation and N-terminal acetylation were set as variable modifications, and carbamidomethylation of cysteines was chosen as a fixed modification. The label-free quantification (LFQ) algorithm was used to quantify the measured peptides and the 'match between runs' option was enabled to quantify peptides with a missing MS_2 spectrum. iBAQ quantification was selected.

Subsequent statistical analysis was performed using Perseus (1.5.5.3) software. Potential contaminants and reverse peptides were excluded, and values were $\log_2$ transformed. iBAQ values of selected proteins were normalized to the median iBAQ values of kindlin-3.

The mass spectrometry proteomics data have been deposited to the ProteomeXchange Consortium via the PRIDE (Perez-Riverol et al., 2019) partner repository with the dataset identifier PXD026711.

Statistical analysis

Data are presented as means±95%c.i. (*in vitro* data) or means±s.d. (*ex vivo* data). Statistical significance was analyzed by applying the following tests: macrophage adhesion, mixed-effects analysis followed by Sidak's multiple comparison test; 9EG7 binding, paired one-way ANOVA followed by Tukey's multiple comparison test; peritonitis, ordinary one-way ANOVA followed by Tukey's multiple comparison test; osteopontin adhesion, ordinary one-way ANOVA followed by Tukey's multiple comparison test; width of podosome belt, ordinary one-way ANOVA followed by Tukey's multiple comparison test; resorption, ordinary one-way ANOVA followed by Tukey's multiple comparison test; bone mineral density and histomorphometry, ordinary one-way ANOVA followed by Tukey's multiple comparison test or two-tailed unpaired Student's *t*-test.

Data availability
The mass spectrometry proteomics data have been deposited to the ProteomeXchange Consortium via the PRIDE partner repository with the dataset identifier PXD026711.

Peer review history
The peer review history is available online at https://journals.biologists.com/jcs/article-lookup/doi/10.1242/jcs.259040

References

Bentmann, A., Kawelke, N., Moss, D., Zentgraf, H., Bala, Y., Berger, I., Gasser, J. A. and Nakchbandi, I. A. (2010). Circulating fibronectin affects bone matrix, whereas osteoblast fibronectin modulates osteoblast function. *J. Bone Miner. Res.* **25**, 706-715. doi:10.1359/jbmr.091011

Bledzka, K., Bialkowska, K., Sossey-Alaoui, K., Vaynberg, J., Pluskota, E., Qin, J. and Plow, E. F. (2016). Kindlin-2 directly binds actin and regulates integrin outside-in signaling. *J. Cell Biol.* **213**, 97-108. doi:10.1083/jcb.201501006

Bottcher, R. T., Veelders, M., Rombaut, P., Faix, J., Theodosiou, M., Stradal, T. E., Rottner, K., Zent, R., Herzog, F. and Fassler, R. (2017). Kindlin-2 recruits paxillin and Arp2/3 to promote membrane protrusions during initial cell spreading. *J. Cell Biol.* **216**, 3785-3798. doi:10.1083/jcb.201701176

Calderwood, D. A., Campbell, I. D. and Critchley, D. R. (2013). Talins and kindlins: partners in integrin-mediated adhesion. *Nat. Rev. Mol. Cell Biol.* **14**, 503-517. doi:10.1038/nrm3624

Cao, H. L., Yan, Q. N., Wang, D., Lai, Y. M., Zhou, B., Zhang, Q., Jin, W. F., Lin, S. M., Lei, Y. M., Ma, L. T. et al. (2020). Focal adhesion protein Kindlin-2 regulates bone homeostasis in mice. *Bone Research* **8**, 2. doi:10.1038/s41413-019-0073-8

Chavakis, E., Carmona, G., Urbich, C., Gottig, S., Henschler, R., Penninger, J. M., Zeiher, A. M., Chavakis, T. and Dimmeler, S. (2008). Phosphatidylinositol-3-kinase-gamma is integral to homing functions of progenitor cells. *Circ. Res.* **102**, 942-949. doi:10.1161/CIRCRESAHA.107.164376

Collin, O., Tracqui, P., Stephanou, A., Usson, Y., Clement-Lacroix, J. and Planus, E. (2006). Spatiotemporal dynamics of actin-rich adhesion microdomains: influence of substrate flexibility. *J. Cell Sci.* **119**, 1914-1925. doi:10.1242/jcs.02838

Cox, J. and Mann, M. (2008). MaxQuant enables high peptide identification rates, individualized p.p.b.-range mass accuracies and proteome-wide protein quantification. *Nat. Biotechnol.* **26**, 1367-1372. doi:10.1038/nbt.1511

Cox, J., Neuhauser, N., Michalski, A., Scheltema, R. A., Olsen, J. V. and Mann, M. (2011). Andromeda: a peptide search engine integrated into the MaxQuant environment. *J. Proteome Res.* **10**, 1794-1805. doi:10.1021/pr101065j

Faccio, R., Takeshita, S., Zallone, A., Ross, F. P. and Teitelbaum, S. L. (2003). c-Fms and the alpha(v)beta(3) integrin collaborate during osteoclast differentiation. *J. Clin. Investig.* **111**, 749-758. doi:10.1172/JCI200316924

Feng, C., Li, Y. F., Yau, Y. H., Lee, H. S., Tang, X. Y., Xue, Z. H., Zhou, Y. C., Lim, W. M., Cornvik, T. C., Ruedl, C. et al. (2012). Kindlin-3 mediates integrin alphaLbeta2 outside-in signaling, and it interacts with scaffold protein receptor for activated-C kinase 1 (RACK1). *J. Biol. Chem.* **287**, 10714-10726. doi:10.1074/jbc.M111.299594

Fu, X. K., Zhou, B., Yan, Q. N., Tao, C., Qin, L., Wu, X. H., Lin, S. X., Chen, S., Lai, Y. M., Zou, X. N. et al. (2020). Kindlin-2 regulates skeletal homeostasis by modulating PTH1R in mice. *Signal Transduct. Target. Ther.* **5**, 297. doi:10.1038/s41392-020-00328-y

Fukuda, K., Bledzka, K., Yang, J., Perera, H. D., Plow, E. F. and Qin, J. (2014). Molecular basis of kindlin-2 binding to integrin-linked kinase pseudokinase for regulating cell adhesion. *J. Biol. Chem.* **289**, 28363-28375. doi:10.1074/jbc.M114.596692

Gao, J., Huang, M., Lai, J., Mao, K., Sun, P., Cao, Z., Hu, Y., Zhang, Y., Schulte, M. L., Jin, C. et al. (2017). Kindlin supports platelet integrin alphaIIbbeta3 activation by interacting with paxillin. *J. Cell Sci.* **130**, 3764-3775.

Georgess, D., Machuca-Gayet, I., Blangy, A. and Jurdic, P. (2014). Podosome organization drives osteoclast-mediated bone resorption. *Cell Adh. Migr.* **8**, 192-204. doi:10.4161/cam.27840

Heuser, J. (2000). The production of 'cell cortices' for light and electron microscopy. *Traffic* **1**, 545-552. doi:10.1034/j.1600-0854.2000.010704.x

Huet-Calderwood, C., Brahme, N. N., Kumar, N., Stiegler, A. L., Raghavan, S., Boggon, T. J. and Calderwood, D. A. (2014). Differences in binding to the ILK complex determines kindlin isoform adhesion localization and integrin activation. *J. Cell Sci.* **127**, 4308-4321.

Jurdic, P., Saltel, F., Chabadel, A. and Destaing, O. (2006). Podosome and sealing zone: Specificity of the osteoclast model. *Eur. J. Cell Biol.* **85**, 195-202. doi:10.1016/j.ejcb.2005.09.008

Klapproth, S., Moretti, F. A., Zeiler, M., Ruppert, R., Breithaupt, U., Mueller, S., Haas, R., Mann, M., Sperandio, M., Fassler, R. et al. (2015). Minimal amounts of kindlin-3 suffice for basal platelet and leukocyte functions in mice. *Blood* **126**, 2592-2600. doi:10.1182/blood-2015-04-639310

Klapproth, S., Bromberger, T., Turk, C., Kruger, M. and Moser, M. (2019). A kindlin-3-leupaxin-paxillin signaling pathway regulates podosome stability. *J. Cell Biol.* **218**, 3436-3454. doi:10.1083/jcb.201903109

Lenter, M., Uhlig, H., Hamann, A., Jeno, P., Imhof, B. and Vestweber, D. (1993). A monoclonal-antibody against an activation epitope on mouse integrin chain-beta(1) blocks adhesion of lymphocytes to the endothelial integrin-alpha(6)beta(1). *Proc. Natl. Acad. Sci. USA* **90**, 9051-9055. doi:10.1073/pnas.90.19.9051

Linder, S. and Aepfelbacher, M. (2003). Podosomes: adhesion hot-spots of invasive cells. *Trends Cell Biol.* **13**, 376-385. doi:10.1016/S0962-8924(03)00128-4

Luxenburg, C., Geblinger, D., Klein, E., Anderson, K., Hanein, D., Geiger, B. and Addadi, L. (2007). The architecture of the adhesive apparatus of cultured osteoclasts: from podosome formation to sealing zone assembly. *PLoS ONE* **2**, e179. doi:10.1371/journal.pone.0000179

Moretti, F. A., Moser, M., Lyck, R., Abadier, M., Ruppert, R., Engelhardt, B. and Fassler, R. (2013). Kindlin-3 regulates integrin activation and adhesion reinforcement of effector T cells. *Proc. Natl. Acad. Sci. USA* **110**, 17005-17010. doi:10.1073/pnas.1316032110

Moretti, F. A., Klapproth, S., Ruppert, R., Margraf, A., Jasmin, W., Pick, R., Scheiermann, C., Sperandio, M., Fassler, R. and Moser, M. (2018). Differential requirement of kindlin-3 for T cell progenitor homing to the non-vascularized and vascularized thymus. *Elife* **7**, e35816. doi:10.7554/eLife.35816.022

Moser, M., Nieswandt, B., Ussar, S., Pozgajova, M. and Fassler, R. (2008). Kindlin-3 is essential for integrin activation and platelet aggregation. *Nat. Med.* **14**, 325-330. doi:10.1038/nm1722

Moser, M., Bauer, M., Schmid, S., Ruppert, R., Schmidt, S., Sixt, M., Wang, H. V., Sperandio, M. and Fassler, R. (2009a). Kindlin-3 is required for beta2 integrin-mediated leukocyte adhesion to endothelial cells. *Nat. Med.* **15**, 300-305. doi:10.1038/nm.1921

Moser, M., Legate, K. R., Zent, R. and Fassler, R. (2009b). The tail of integrins, talin, and kindlins. *Science* **324**, 895-899. doi:10.1126/science.1163865

Perez-Riverol, Y., Csordas, A., Bai, J. W., Bernal-Llinares, M., Hewapathirana, S., Kundu, D. J., Inuganti, A., Griss, J., Mayer, G., Eisenacher, M. et al. (2019). The PRIDE database and related tools and resources in 2019: improving support for quantification data. *Nucleic Acids Res.* **47**, D442-D450. doi:10.1093/nar/gky1106

Pfaff, M. and Jurdic, P. (2001). Podosomes in osteoclast-like cells: structural analysis and cooperative roles of paxillin, proline-rich tyrosine kinase 2 (Pyk2) and integrin alphaVbeta3. *J. Cell Sci.* **114**, 2775-2786. doi:10.1242/jcs.114.15.2775

Qin, L., Fu, X. K., Ma, J., Lin, M. X., Zhang, P. J., Wang, Y. S., Yan, Q. N., Tao, C., Liu, W., Tang, B. et al. (2021). Kindlin-2 mediates mechanotransduction in bone by regulating expression of Sclerostin in osteocytes. *Commun. Biol.* **4**, 402. doi:10.1038/s42003-021-01950-4

Rappsilber, J., Ishihama, Y. and Mann, M. (2003). Stop and go extraction tips for matrix-assisted laser desorption/ionization, nanoelectrospray, and LC/MS sample pretreatment in proteomics. *Anal. Chem.* **75**, 663-670. doi:10.1021/ac026117i

Saftig, P., Hunziker, E., Everts, V., Jones, S., Boyde, A., Wehmeyer, O., Suter, A. and von Figura, K. (2000). Functions of cathepsin K in bone resorption - Lessons from cathepsin K deficient mice. *Cellular Peptidases in Immune Functions and Diseases 2* **477**, 293-303. doi:10.1007/0-306-46826-3_32

Schmidt, S., Nakchbandi, I., Ruppert, R., Kawelke, N., Hess, M. W., Pfaller, K., Jurdic, P., Fassler, R. and Moser, M. (2011). Kindlin-3-mediated signaling from multiple integrin classes is required for osteoclast-mediated bone resorption. *J. Cell Biol.* **192**, 883-897. doi:10.1083/jcb.201007141

Takito, J., Inoue, S. and Nakamura, M. (2018). The sealing zone in osteoclasts: a self-organized structure on the bone. *Int. J. Mol. Sci.* **19**, 984. doi:10.3390/ijms19040984

Theodosiou, M., Widmaier, M., Bottcher, R. T., Rognoni, E., Veelders, M., Bharadwaj, M., Lambacher, A., Austen, K., Muller, D. J., Zent, R. et al. (2016). Kindlin-2 cooperates with talin to activate integrins and induces cell spreading by directly binding paxillin. *Elife* **5**, e10130. doi:10.7554/eLife.10130

Udagawa, N., Takahashi, N., Akatsu, T., Tanaka, H., Sasaki, T., Nishihara, T., Koga, T., Martin, T. J. and Suda, T. (1990). Origin of osteoclasts - mature monocytes and macrophages are capable of differentiating into osteoclasts under a suitable microenvironment prepared by bone marrow-derived stromal cells. *Proc. Natl. Acad. Sci. USA* **87**, 7260-7264. doi:10.1073/pnas.87.18.7260

Ussar, S., Wang, H. V., Linder, S., Fässler, R. and Moser, M. (2006). The Kindlins: subcellular localization and expression during murine development. *Exp. Cell Res.* **312**, 3142-3151. doi:10.1016/j.yexcr.2006.06.030

van den Dries, K., Linder, S., Maridonneau-Parini, I. and Poincloux, R. (2019). Probing the mechanical landscape-new insights into podosome architecture and mechanics. *J. Cell Sci.* **132**, jcs236828. doi:10.1242/jcs.236828

Wu, C. Y., Jiao, H. L., Lai, Y. M., Zheng, W., Chen, K., Qu, H., Deng, W. M., Song, P. P., Zhu, K., Cao, H. L. et al. (2015). Kindlin-2 controls TGF-beta signalling and Sox9 expression to regulate chondrogenesis. *Nat. Commun.* **6**, 7531. doi:10.1038/ncomms8531

Xue, Z. H., Feng, C., Liu, W. L. and Tan, S. M. (2013). A role of kindlin-3 in integrin alpha M beta 2 outside-in signaling and the Syk-Vav1-Rac1/Cdc42 signaling axis. *PLoS ONE* **8**, e56911. doi:10.1371/journal.pone.0056911
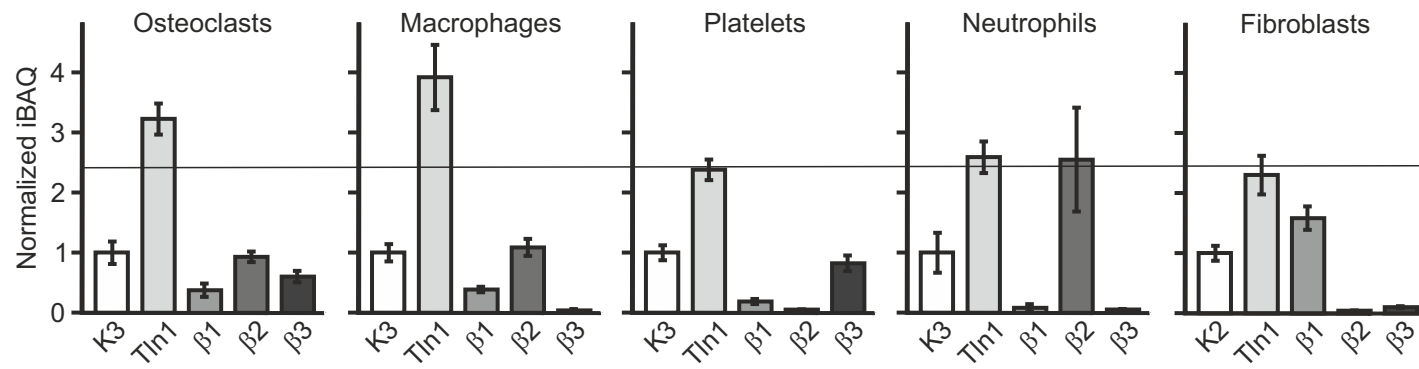
**Fig. S1. Talin is more abundant compared to kindlin in osteoclasts and macrophages than in platelets, neutrophils and fibroblasts**.

Quantification of the protein levels of talin-1, kindlin-2/3 and integrin subunits β1/2/3 in different cell types by whole proteome mass spec analyses. All values are given in relation to the amount of kindlin-3. Osteoclasts: N=3. Macrophages, platelets, fibroblasts: N=4. Neutrophils: N=2.
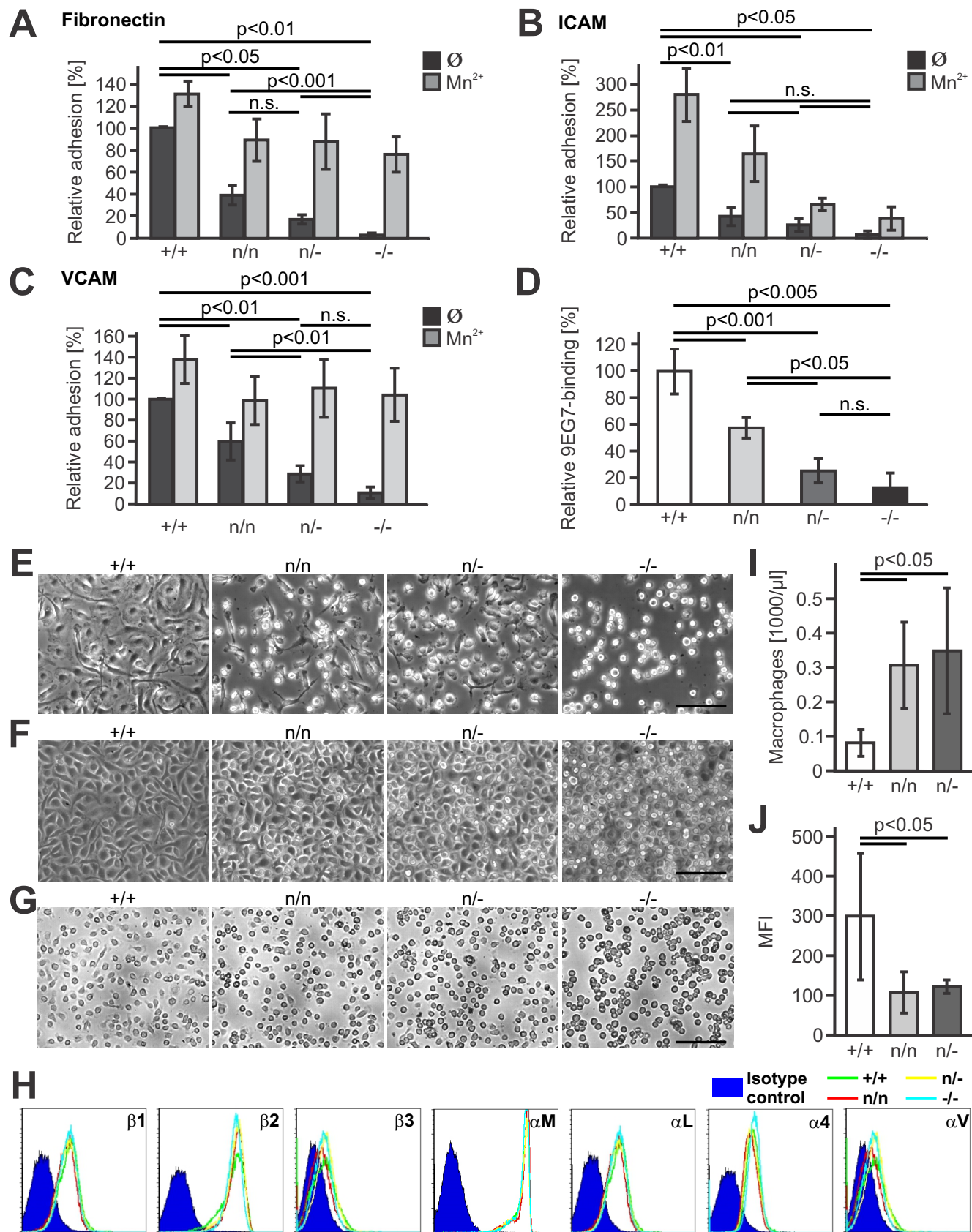
Fig. S2. Integrin activation in macrophages is reduced in a kindlin-3-dose-dependent manner.
(A-C) Static adhesion of +/+, n/n, n/- and -/- macrophages on fibronectin (A), ICAM (B) and VCAM
(C) in the presence or absence of $MnCl_2$. Values are given as mean ± c.i. N≥6 for fibronectin and
ICAM, N≥3 for VCAM. (D) Activation level of β1-integrins, assessed as relative binding of 9EG7
antibody. Values are given as mean ± c.i. N≥5. (E-G) +/+, n/n, n/- and -/- macrophages plated on
glass (E), cell culture-treated plastic (F) and fibronectin coated bacterial plastic (G). Size bars 100
µm. (H) Surface expression of the integrin subunits β1, β2, β3, αM, αL, α4, α5 and αV on +/+, n/n,
n/- and -/- macrophages analysed by FACS. (I) Number of macrophages in the peritoneal lavage
collected 24 h after initiating peritonitis. Values are given as mean ± c.i. N=5. (J) Phagocytic capacity
of peritoneal macrophages isolated 24 h after initiating peritonitis. Values are given as mean ± c.i.
N=5.
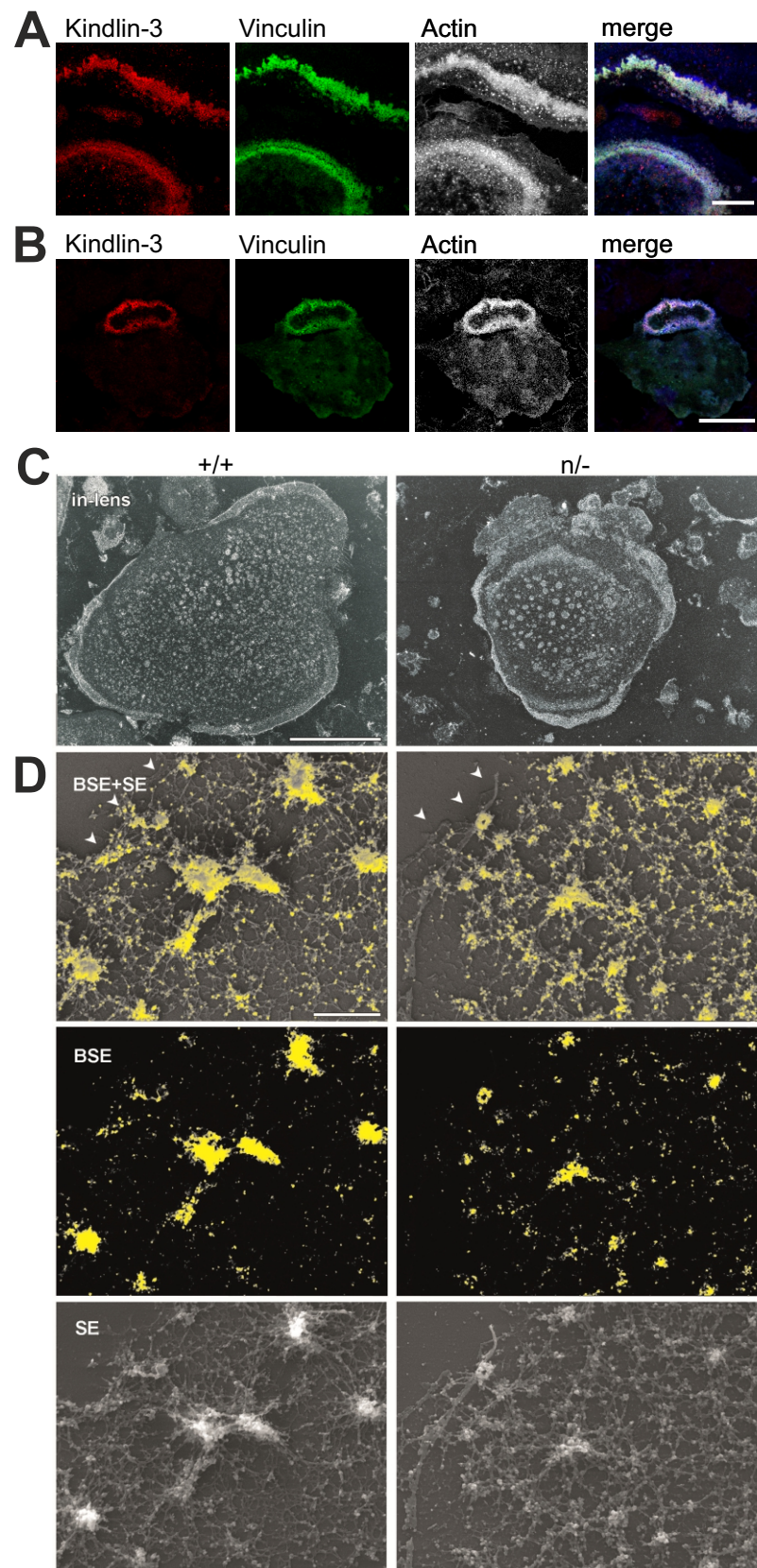
Fig. S3. Kindlin-3 localizes to podosome belts and sealing zones. (A,B) Wild-type osteoclast-like cells differentiated on glass (A) or mineralized matrix (B) immunofluorescently labelled for kindlin-3 (red), vinculin (green) and actin (white, in merge blue). Size bars 20 µm. (C,D) Morphology of podosome belts differs between +/+ and n/- osteoclast-like cells. (C) Scanning electron microscopy of ventral membrane preparations; overviews. Size bar 50 µm. (D) BSE + SE signal mixing shows actin immunogold patterns (yellow) complemented with morphology of the podosome belt (arrow heads mark cell border). Size bar 1 µm.
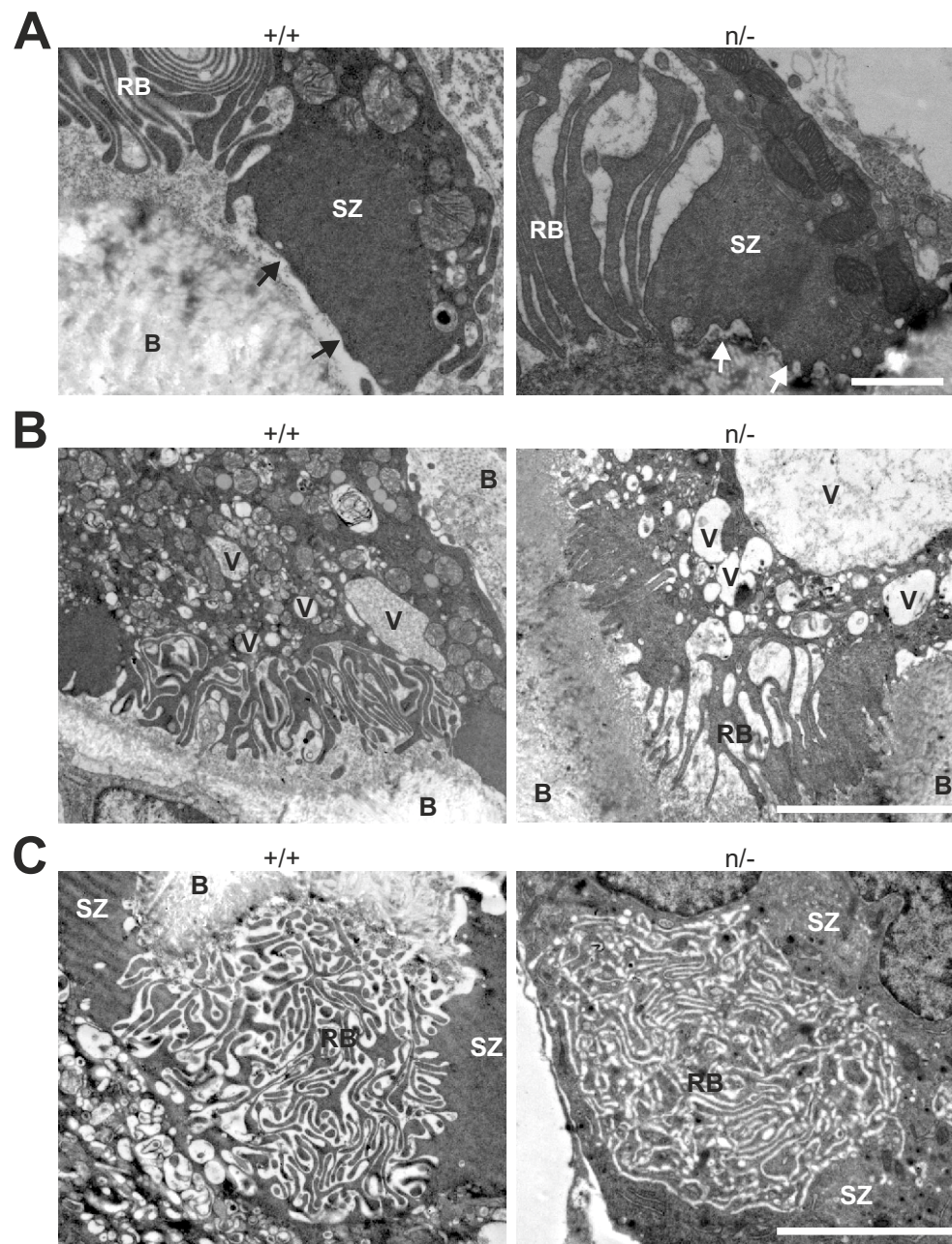
Fig. S4. Sealing zones and ruffled borders of control and hypomorphic osteoclasts are structurally different. Electron microscopy on bone ultrasections in +/+ and n/- mice at postnatal age of 7 days. Size bars 1 µm (A) and 5 µm (B and C). B, bone. SZ, sealing zone. RB, ruffled border. V, vesicle.

Table S1. Key Resources

Reagent type (species) or resource	Designation	Source or reference	Identifiers	Additional information
genetic reagent *(M.musculus)*	*Fermt3⁻ᐟ⁻*	PMID: 18278053	RRID: MGI:2147790	Dr. Reinhard Fässler (Max Planck Institute of Biochemistry)
genetic reagent *(M.musculus)*	*Fermt3ⁿ⁻*	PMID: 26438512	RRID: MGI:3785479	Dr. Reinhard Fässler (Max Planck Institute of Biochemistry)
antibody	anti-CD11b-biotin	BD Pharmingen	Cat. #: 557395; RRID: AB_2296385	FACS (1:200)
antibody	anti-CD11b-PE	BD Pharmingen	Cat. #: 557395; RRID: AB_2296385	FACS (1:300)
antibody	anti-CD11b-PerCP-Cy5.5	eBioscience	Cat. #: 45-0112-80 ; RRID: AB_953560	FACS (1:200)
antibody	anti-CD16/CD32	BD Pharmingen	Cat. #: 553142; RRID: AB_394657	FACS (1:400)
antibody	anti-CD45-APC/Cy7	Biolegend	Cat. #: 103116; RRID: AB_312981	FACS (1:200)
antibody	anti-CD115-APC	Biolegend	Cat. #: 135510; RRID: AB_2085221	FACS (1:200)
antibody	anti-Cathepsin K	Merck Millipore	Cat. #: IM55, RRID: AB_2230159	IF (1:100)
antibody	anti-F4/80-eFluor450	eBioscience	Cat. #: 48-4801-82, RRID: AB_1548747	FACS (1:200)
antibody	mouse anti-GAPDH	Merck Millipore	Cat. #: CB1001; RRID: AB_2107426	WB (1:20.000)
antibody	anti-Gr-1-PE	eBioscience	Cat. #: 12-5931-82; RRID: AB_466045	FACS (1:200)
antibody	alexa-fluor-488-conjugated anti-mouse IgG	Thermo Fisher Scientific	Cat. #: A-11001; RRID: AB_2534069	IF (1:300)
antibody	alexa-fluor-546-conjugated anti-mouse IgG	Thermo Fisher Scientific	Cat. #: A-11003; RRID: AB_2534071	IF (1:300)
antibody	Peroxidase AffiniPure goat anti-mouse IgG (H+L)	Jackson Immunoresearch	Cat. #: 115-035-003; RRID: AB_10015289	WB (1:15.000)
antibody	alexa-fluor-488-conjugated anti-rabbit IgG	Thermo Fisher Scientific	Cat. #: A-11034; RRID: AB_2576217	IF (1:300)
antibody	alexa-fluor-546-conjugated anti-rabbit IgG	Thermo Fisher Scientific	Cat. #: A-11010; RRID: AB_2534077	IF (1:300)
antibody	Peroxidase AffiniPure goat anti-rabbit IgG (H+L)	Jackson Immunoresearch	Cat. #: 111-035-045; RRID: AB_2337938	WB (1:15.000)

antibody	anti-Integrin α4-PE	BD Pharmingen	Cat. #: 553157; RRID: AB_394670	FACS (1:200)
antibody	anti-Integrin αL-PE	BD Pharmingen	Cat. #: 553121; RRID: AB_394637	FACS (1:200)
antibody	anti-Integrin αM-PE	BD Pharmingen	Cat. #: 557395; RRID: AB_2296385	FACS (1:300)
antibody	anti-Integrin αM-biotin	eBioscience	Cat. #: 12-0112-85; RRID: AB_465549	FACS (1:200)
antibody	anti-Integrin αV-PE	BD Pharmingen	Cat. #: 551187, RRID: AB_394088	FACS (1:200)
antibody	anti-Integrin β1 (clone 9EG7)	BD Pharmingen	Cat. #: 553715, RRID:AB_395001	FACS (1:100)
antibody	anti-Integrin β1-PE	Biolegend	Cat. #: 102207; RRID: AB_312884	FACS (1:200)
antibody	anti-Integrin β2-PE	BD Pharmingen	Cat. #: 553293; RRID: AB_394762	FACS (1:200)
antibody	anti-Integrin β3-PE	eBioscience	Cat. #: 12-0611-81; RRID: AB_465717	FACS (1:200)
antibody	rabbit anti-Kindlin-3	Markus Moser (MPI of Biochemistry)		WB (1:3,000) IF (1:100)
antibody	mouse anti-paxillin	Thermo Fisher Scientific	Cat. #: 610051, RRID: AB_397463	WB (1:5,000)
antibody	rabbit anti-paxillin	abcam	Cat. #: ab32084, RRID: AB_779033	IF (1:300)
antibody	rabbit anti-paxillin pY31	Thermo Fisher Scientific	Cat. #: 44-720G; RRID: AB_2533732	WB (1:1,000)
antibody	rabbit anti-paxillin pY118	Thermo Fisher Scientific	Cat. #: 44-722G, RRID:AB_2533733	WB (1:1,000)
antibody	rabbit anti-Pyk2	Cell Signaling Technology	Cat. #: 3292, RRID: AB_2174097	WB (1:1,000)
antibody	rabbit anti-phospho-Pyk2 Y402	Cell Signaling Technology	Cat. #: 3291, RRID: AB_2300530	WB (1:1,000)
antibody	mouse anti-talin	Sigma-Aldrich	Cat. #: T3287; RRID: AB_477572	WB (1:20.000), IF (1:500)
antibody	mouse anti-vinculin	Sigma-Aldrich	Cat. #: V9131, RRID: AB_477629	IF (1:500)
peptide, recombinant protein	Fibronectin Bovine plasma	Merck Millipore	Cat. #: 341631	5 µg/ml

peptide, recombinant protein	recombinant human ICAM-1	R&D Systems	Cat. #: ADP4-200; Accession #: CAA30051	4 µg/ml
peptide, recombinant protein	recombinant mouse Osteopontin	R&D Systems	Cat. #: 441-OP-050/CF; Accession #: Q547B5	2 µg/ml
peptide, recombinant protein	recombinant mouse TNF-α	R&D Systems	Cat. #: 410-MT-025/CF; Accession #: P06804	
peptide, recombinant protein	recombinant human VCAM-1	R&D Systems	Cat. #: ADP5-200; Accession #: P19320-1	4 µg/ml
chemical compound, drug	Alexa Fluor 647 Antibody labeling kit	Thermo Fisher Scientific	Cat. #: A20186	
chemical compound, drug	Cathepsin K Activity Fluorometric Assay Kit	BioVision	Cat. #: K141-100	
chemical compound, drug	cOmplete EDTA-free Protease Inhibitor Cocktail	Sigma-Aldrich	Cat. #: 4693132001	
chemical compound, drug	FACS Lysing Solution	BD Biosciences	Cat. #: 349202	
chemical compound, drug	recombinant mouse M-CSF	tebu-bio	Cat. #: 315-02-B	
chemical compound, drug	Alexa Fluor 488 Phalloidin	Thermo Fisher Scientific	Cat. #: A12379	IF (1:500)
chemical compound, drug	Alexa Fluor 647 Phalloidin	Thermo Fisher Scientific	Cat. #: A22287, RRID: AB_2620155	IF (1:40)
chemical compound, drug	Phosphatase Inhibitor Cocktail 2	Sigma-Aldrich	Cat. #: P5726	
chemical compound, drug	Phosphatase Inhibitor Cocktail 3	Sigma-Aldrich	Cat. #: P0044	
chemical compound, drug	pHrodo Green *E.coli* BioParticles Conjugate	Thermo Fisher Scientific	Cat. #: P35366	
chemical compound, drug	recombinant mouse sRANKL	tebu-bio	Cat. #: 315-11-B	
chemical compound, drug	Streptavidin-Cy5	Jackson ImmunoResearch	Cat. #: 016-170-084, RRID: AB_2337245	FACS (1:400)
software, algorithm	FlowJo	BD Biosciences	RRID:SCR_008520	
software, algorithm	ImageJ	National Institute of Health	RRID:SCR_003070	
software, algorithm	MetaMorph	Molecular Devices	RRID:SCR_002368	
software, algorithm	Perseus	Max-Planck-Institute of Biochemistry	RRID:SCR_015753	
software, algorithm	Photoshop	Adobe	RRID:SCR_014199	
other	Glass Bottom Microwell Dishes	MatTek Corporation	Cat. #: P35G-1.5-20-C	
other	BioCoat Osteologic Discs	BD Biosciences	Cat. #: 354610	